Int. J. Heat Mass Transfer. Vol. 35, No. 10, pp. 2465–2474, 1992
Printed in Great Britain

0017-9310/92 $5.00 + 0.00

Analysis of microchannels for integrated cooling

AREL WEISBERG and HAIM H. BAU†
Department of Mechanical Engineering and Applied Mechanics, University of Pennsylvania, Philadelphia, PA 19104-6315, U.S.A.

and

J. N. ZEMEL
Department of Electrical Engineering, University of Pennsylvania, Philadelphia, PA 19104-6315, U.S.A.

(*Received* 7 *August* 1991 *and in final form* 4 *November* 1991)

Abstract—Recent advances in the precision machining of small channels have made possible the use of such micro-channels in ultra compact, very efficient heat exchangers, which capitalize on the channels' large surface area to volume ratio to transport high heat fluxes with small thermal resistances. For instance, such micro-channels can be fabricated right into the back of electronic chips to effectuate the cooling of these chips. In this paper, we analyze such heat exchangers by solving numerically a conjugate heat transfer problem consisting of the simultaneous determination of the temperature fields in both the solid substrate and the fluid. Additionally, we present a design algorithm for the selection of the heat exchanger's dimensions.

1. INTRODUCTION

ADVANCES in microfabrication technology allow the manufacturing of micro-heat exchangers consisting of multiple minute flow conduits with hydraulic diameters ranging from 10 to 10^3 μm. These micro-heat exchangers are characterized by extremely high surface area per unit volume of working fluid, low thermal resistance, low mass, low volume and low inventory of working fluid. Their main disadvantage is their susceptibility to fouling which mandates the use of very clean working fluids. Although micro-heat exchangers may have numerous potential applications, their use thus far has been advocated primarily for the cooling of electronic chips [1, 2], cryocoolers for cooling sensors and diode lasers [3] and Stirling engines [4].

The flow channels or interrupted fins are typically fabricated on thin sheets of silicon, metal or other suitable materials. The individual sheets can be either used separately to form flat plate heat exchangers ([1, 2] and Figs. 1 and 2 below) or they can be stacked and bonded to form parallel, counter, or cross-flow heat exchangers [4, 5]. The channels and/or fins can be manufactured on the sheets' surfaces utilizing photolithographic techniques or precision cutting with micro-tools [6]. Recently, Hoopman [7] reported a unique fabrication technology which allows one to introduce two and three dimensional flow structures of various cross-sections either onto the surface or inside the material.

In this study, we focus on flat plate heat exchangers of the type studied experimentally and theoretically in

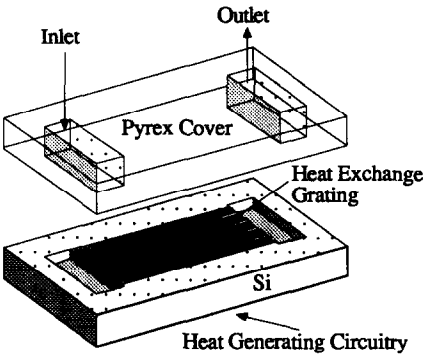

FIG. 1. Schematic description of the heat exchanger. Fluid flows in channels fabricated on top of the wafer. The channels are covered with a pyrex plate.

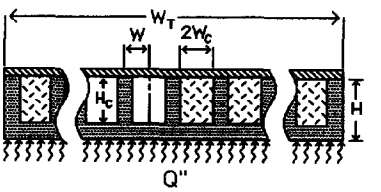

FIG. 2. A cross-section of the heat exchanger is shown with the dimensions used in the analysis.

† Author to whom all correspondence should be addressed.

NOMENCLATURE

A	channel's aspect ratio ($H_c/2W_c$)
C_p	fluid's thermal capacity
d_H	non-dimensional hydraulic diameter
D_H	channel's hydraulic diameter [m]
h	non-dimensional wafer's thickness ($=H/H_c$)
H	chip's height [m]
H_c	channel's height [m]
k_s	solid's thermal conductivity [W m^{-1} K^{-1}]
k_f	fluid's thermal conductivity [W m^{-1} K^{-1}]
L	channel's length [m]
n	number of flow conduits
$\hat{n}$	specified medium's outwardly directed normal vector
Nu_L	local Nusselt number
P	pressure [N m^{-2}]
Q''	uniform heat flux [W m^{-2}]
Q_c	axial conduction in the substrate [W]
Q	total heat flow into the substrate [W]
r	non-dimensional thermal resistance of a cross-section
R^*	overall thermal resistance [K W^{-1}]
R	thermal resistance of a cross-section
Re	Reynolds number
T	temperature [K]
T_B	fluid's bulk temperature [K]
$\overline{T(h, z)}$	average surface temperature at location z [K]
u	non-dimensional velocity field
$\bar{U}$	cross-sectional averaged fluid velocity [m s^{-1}]
W	half the distance between adjacent channels [m]
w_c	non-dimensional half channel width (W_c/H_c)
W_c	half channel's width [m]
W_T	chip's width [m]
x, y, z	Cartesian co-ordinates.

Greek symbols

θ	non-dimensional temperature
$\bar{\theta}$	average non-dimensional surface temperature at location z
μ	dynamic viscosity [kg m^{-1} s^{-1}]
ρ_f	fluid's density [kg m^{-3}].

ref. [8] and which may be used for electronic-chip cooling. The heat exchangers consist of rectangular channels fabricated in a silicon wafer and capped with a pyrex plate (Figs. 1 and 2). The wafer's surface is uniformly heated to simulate Joule heating and the working fluid is water. Similar channels containing gases and other liquids have been studied experimentally [9–14]. For additional references and a lucid review of the pertinent literature, we refer the reader to Philips [15].

Tuckerman [8], Keyes [16], and Samalam [17] have theoretically studied heat transfer to microchannels. Their works have included a number of simplifications and approximations, most notably: (i) the heat transfer coefficients along the channels' walls were assumed to be uniform and were arbitrarily chosen; (ii) all the heat transport occurs through the vertical fins, the temperature of which was assumed to vary only in the vertical direction in each cross-section; and (iii) the fluid temperature at each cross-section was assumed to be uniform or, at most, a function of one coordinate. In other words, the aforementioned authors have used classical fin analysis; but the inadequacy of fin analysis for this case has been demonstrated by Sparrow *et al.* [18], who studied numerically heat transfer in a shrouded fin array.

In this study, we eliminate many of the approximations used by previous researchers and solve a conjugate heat transfer problem which consists of the simultaneous calculation of the heat transport in the solid and the liquid. Our objectives are to check the validity of the various approximations employed by previous researchers, obtain relevant heat transfer correlations and devise an algorithm for the heat exchangers' design.

2. MATHEMATICAL MODEL

An integrated cooling system is typically manufactured by machining a large number ($O(10^2)$) of channels onto the back of a silicon chip (Fig. 1). The channels are sealed by hermetically bonding a glass or silicon plate on top of the channels. The cooling fluid is supplied into and removed from the channels through holes drilled in the cover plate. The shape of the channels depends on a variety of factors such as the crystallographic nature of the material used and the machining techniques employed. For example, etching $\langle 100 \rangle$ and $\langle 110 \rangle$ silicon in KOH solutions will result, respectively, in channels with trapezoidal and rectangular cross-sections.

For the purposes of this paper, we assume that all the channels have a uniform, rectangular cross-section of width $2W_c$, height H_c, hydraulic diameter $D_H = 4W_cH_c/(2W_c+H_c)$, and length L. The distance between the centers of adjacent channels is $2W$ and the thickness of the wafer is H (Fig. 2). Since the top plate is often made out of glass, the thermal conductivity of which is about two orders of magnitude lower than that of silicon, we assume the top boundary

to be insulated. This is a conservative assumption which will lead to a slight overestimation of the overall thermal resistance. A more precise analysis would require information about the thermal interaction between the top of the glass plate and its environment. The exact nature of this interaction depends on the packaging of the electronic circuits and is not likely to be generic.

The channels' surfaces are assumed to be smooth. In a parallel work [19], we demonstrated that channels with surface roughness (peak to valley) smaller than 1% of the channel's height can, indeed, be machined. The thermal conductivities of the solid and the fluid are k_s and k_f, respectively. Uniform heat flux Q'' is applied to the wafer's top.

Taking advantage of symmetry and neglecting end effects (which we justify on account of the large number of channels employed), our computations center on a unit cell consisting of half a channel and the surrounding solid. Figure 3 depicts the computational domain, the governing equations, and the boundary conditions. We use the channel's height, H_c, as a length scale and the cross-sectionally averaged velocity ($\bar{U}$) as a velocity scale. We adopt the convention that upper and lower case letters represent, respectively, dimensional and non-dimensional quantities. For example, the non-dimensional height and half-width of the channel are denoted h_c ($=1$) and $w_c = (W_c/H_c)$, respectively, and the wafer's thickness is $h = (H/H_c > 1)$.

As typically $L/D_H \gg 1$ and the Reynolds number (Re) is relatively low (on the order of 10^2), we assume laminar, fully developed (hydraulically and thermally) flow. For example, typical dimensions of the channel are $L \sim 10^4$ μm and $D_H \sim 50$ μm, resulting in $L/D_H \sim 200$ and a hydraulic development length of 250 μm (2.5% of channel's length) for $Re \sim 100$. In situations in which entrance effects may be important, our model would overestimate the actual thermal resistance.

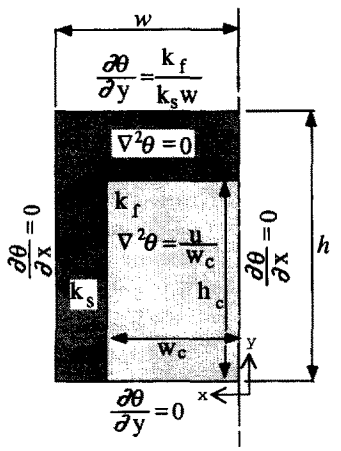

FIG. 3. A computational 'cell' obtained utilizing symmetry is shown together with the governing equations and boundary conditions.

The dimensional average velocity $\bar{U}$ and the non-dimensional velocity field $u(x, y)$ are obtained from the classical expressions for fully developed, laminar flow in a rectangular duct with aspect ratio $A = H_c/2W_c = 1/2w_c > 1$ [20]

$$\bar{U} = \frac{H_c^2}{12\mu}\left(\frac{-\mathrm{d}P}{\mathrm{d}Z}\right)\left[1 - \frac{192A}{\pi^5}\sum_{n=1,3,5,\ldots}^{\infty}\frac{\tanh\left(2\frac{n\pi}{A}\right)}{\pi^5}\right],$$

and

$$u(x,y) = \left\{48\pi^{-3}\sum_{i=1,3,5,\ldots}^{\infty}(-1)^{(i-1)/2} \times\left[1-\frac{\cosh(i\pi x)}{\cosh(i\pi w_c)}\right]\frac{\cos(i\pi(y-0.5))}{i^3}\right\}\Bigg/ \left[1-\frac{96}{\pi^5 w_c}\sum_{i=1,3,5,\ldots}^{\infty}\frac{\tanh(i\pi w_c)}{i^5}\right]. \quad (1)$$

In the above, P is the pressure, μ is the dynamic viscosity, and (x, y, z) are Cartesian coordinates. The coordinates (x, y) are depicted in Fig. 3. The coordinate z is aligned in the streamwise direction.

In our model, we also neglect the axial conduction both in the substrate and the fluid. The axial conduction in the substrate (Q_c)

$$\frac{Q_c}{Q} = \frac{k_s A_s \frac{\mathrm{d}T_B}{\mathrm{d}Z}}{Q''WL} = \frac{k_s}{L\rho_f C_p \bar{U}}\left(\frac{WH}{W_c H_c} - 1\right) \quad (2)$$

is estimated to be much smaller than 1% of the total heat flow (Q). In equation (2), Q'' is the uniform heat flux at the wafer's surface; $2(WH - W_cH_c)$ is the solid's cross-sectional area (Fig. 3); ρ_f and C_p are, respectively, the fluid's density and specific heat; $T_B(Z)$ is the fluid's bulk temperature; and

$$\frac{\mathrm{d}T_B}{\mathrm{d}Z} = \frac{Q''}{\rho_f C_p \bar{U}}\frac{W}{W_c H_c}, \quad (3)$$

where the non-dimensional temperature

$$\theta(x,y) = \frac{k_f}{WQ''}[T(x,y,z) - T_B(z)]$$

and the dimensional temperature is $T(x, y, z)$. In equation (2), we have implicitly assumed that, due to the small thermal resistance between the solid and the fluid, the axial temperature gradient in both is about the same.

The temperature field satisfies the equation:

$$\frac{\partial^2\theta^*}{\partial x^2} + \frac{\partial^2\theta^*}{\partial y^2} = \begin{cases}\dfrac{u(x,y)}{w_c} & \text{in the fluid}\\ 0 & \text{in the solid}\end{cases}, \quad (4)$$

with the external boundary conditions as depicted in Fig. 3. The temperature and flux continuity across the solid–liquid interfaces are

$$\frac{k_s}{k_f}\left(\frac{\partial\theta^*}{\partial\hat{n}}\right)_{\text{solid}} = -\left(\frac{\partial\theta^*}{\partial\hat{n}}\right)_{\text{fluid}}, \tag{5}$$

where $\hat{n}$ is the specified medium's outwardly directed normal vector at the solid–fluid interface.

Note that we use in equation (4) a new variable θ^* which is different from θ. This is because equation (4) and the corresponding boundary conditions (Fig. 3) yield a temperature distribution which is invariant to the addition of a constant. We enforce uniqueness by utilizing the definition of the non-dimensional temperature, which implies $\theta_B = 0$. Accordingly, $\theta(x, y) = \theta^*(x, y) - \theta_c$, where

$$\theta_c = \frac{1}{W_c}\int_0^{W_c} dx \int_0^1 dy\, u(x, y)\theta^*(x, y). \tag{6}$$

Once the temperature profile $\theta(x, y)$ is known, all the relevant heat transfer quantities may be computed. The local Nusselt number (Nu_L) is given by the formula:

$$Nu_L = \frac{H_c}{T_{sf} - T_B}\left(\frac{\partial T}{\partial\hat{n}}\right)_{sf} = \left(\frac{1}{\bar{\theta}}\frac{\partial\theta}{\partial\hat{n}}\right)_{sf}, \tag{7}$$

where subscript (sf) denotes the solid–fluid interface. For design purposes, one is typically interested in the overall thermal resistance,

$$R^* = \frac{\overline{T(h, L)} - T_B(0)}{Q'' W_T L} = R + \frac{W}{\rho_f C_p \bar{U} W_c H_c W_T}, \tag{8}$$

expressed in units of (K W^{-1}) and based on the temperature difference between the wafer's surface temperature at the channel's exit and the inlet bulk temperature. In the above,

$$R = \frac{\overline{T(h, z)} - T_B(z)}{Q'' W_T L} = \frac{\overline{\theta_{surf}}}{k_f L}\frac{W}{W_T},$$

where the overbar denotes averaging in the x direction along the wafer's surface at a given axial location z. As the magnitude of R^* depends on the flow rate, we shall present our results in terms of the cross-sectional thermal resistance R, which depends only on the cross-sectional geometry and the fluid's and solid's thermophysical properties or R's non-dimensional counterpart

$$r = \frac{W_T k_f L R}{H_c} = w\overline{\theta_{surf}}. \tag{9}$$

We note in passing that occasionally one may prefer to define the thermal resistance based on the maximal surface temperature rather than the average one. Due to the high thermal conductivity of the silicon, the difference between these two resistance definitions is likely to be small.

3. SOLUTION PROCEDURE AND NUMERICAL CODE VERIFICATION

Using central differencing, we calculated numerically the temperature field (θ). The resulting algebraic equations were solved iteratively using the successive over relaxation method to speed up the scheme's convergence. The iterations were truncated once the convergence criterion

$$\operatorname{Max}_{i,j}\left|\frac{\theta^m_{i,j} - \theta^{m-1}_{i,j}}{\theta^{*m}_{i,j} - \theta^m_c}\right| \leqslant \varepsilon \sim 10^{-6}, \tag{10}$$

at the mth iteration was satisfied. We used a uniform grid whose size was chosen so as to assure grid-independent solutions. The number of needed grid points varied according to the geometrical configuration of the cell. For illustration purposes, we depict in Fig. 4 the total number of grid points needed as a function of various geometrical factors. Typically, the number of grid points and the number of iterations increased with increasing aspect ratio. Often a relatively large number of iterations (on the order of 10^4) was needed to satisfy the convergence criterion (10). We surmise that this slow convergence is due to the large difference between the solid's and the fluid's thermal conductivities.

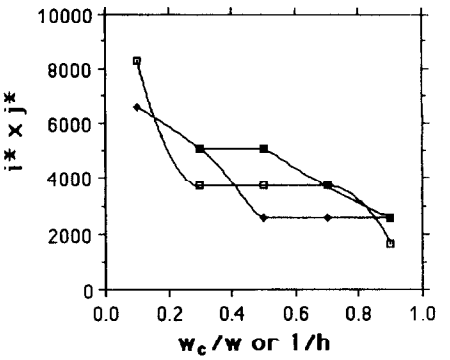

FIG. 4. The number of grid points required for convergence. The hollow squares and diamonds depict cases involving channel aspect ratios of 4 and 6, respectively, as a function of w_c/w, with $h = 1.11$. The solid squares depict the case of $w_c/w = 0.3$, as a function of h^{-1}, and an aspect ratio of 3. $k_s/k_f = 243$.

Kelkar [21], who also encountered slow convergence while solving iteratively a conjugate heat transfer problem in media with large differences in thermal conductivity, suggested that the problem could be alleviated through the use of a procedure somewhat similar to a multi-grid technique. Rather than attempting this, we tried to use a direct inversion [22]. Unfortunately, due to machine memory limitations, we were able to employ the inversion technique only for cases with a relatively small number of grid points. However, as the development of an efficient numerical procedure is not central to this paper, we merely point out the need for such a code.

In addition to verifying that the code is self-consistent by demonstrating that the numerical predictions are independent of the number of both grid points and iterations, we compared the results with known solutions for some special cases. We began by

imposing a uniform, fixed temperature at the solid–fluid interface. This is the limiting case of $k_s/k_f \to \infty$. Our results agreed within 1% with those published in Shah and London [23]. Next, we looked at the special case of the liquid and the solid having the same thermal conductivity ($k_s = k_f$). It is easy to construct an analytic solution in series form for this case. For example, the temperature field for a plug flow ($u = 1$) is given by

$$\theta = \theta^* - \theta_c, \tag{11}$$

where

$$\theta^*(x,y) = \frac{y^2}{2wh} - \frac{2w^2}{w_c h\pi^3}\sum_{m=1}^{\infty}\frac{1}{m^3}\sin\left(\frac{\pi m w_c}{w}\right)\cos\left(\frac{\pi m x}{w}\right) - \frac{2h^2}{w\pi^3}\sum_{n=1}^{\infty}\frac{1}{n^3}\sin\left(\frac{\pi n}{h}\right)\cos\left(\frac{\pi n y}{h}\right) - \frac{4}{w_c\pi^4} \times \sum_{m=1}^{\infty}\sum_{n=1}^{\infty}\frac{\sin\left(\frac{\pi m w_c}{w}\right)\cos\left(\frac{\pi m x}{w}\right)\sin\left(\frac{\pi n}{h}\right)\cos\left(\frac{\pi n y}{h}\right)}{mn\left(\left(\frac{m}{w}\right)^2 + \left(\frac{n}{h}\right)^2\right)}, \tag{12}$$

and

$$\theta_c = \frac{1}{6wh} - \frac{2w^3}{w_c^2 h\pi^4}\sum_{m=1}^{\infty}\frac{1}{m^4}\sin^2\left(\frac{\pi m w_c}{w}\right) - \frac{2h^3}{w\pi^4}\sum_{n=1}^{\infty}\frac{1}{n^4}\sin^2\left(\frac{\pi n}{h}\right) - \frac{4wh}{w_c^2\pi^6}\sum_{m=1}^{\infty}\sum_{n=1}^{\infty}\frac{\sin^2\left(\frac{\pi m w_c}{w}\right)\sin^2\left(\frac{\pi n}{h}\right)}{m^2n^2\left(\left(\frac{m}{w}\right)^2 + \left(\frac{n}{h}\right)^2\right)}. \tag{13}$$

Results obtained from the numerical simulation and the analytic solution were in excellent agreement (less than 0.05% difference except in a narrow region where the temperature's magnitude was close to zero).

4. RESULTS AND DISCUSSION

We computed the temperature distribution, $\theta(x, y)$, in the liquid and the solid for various channel geometries. All the results presented in this section are for a silicon substrate ($k_s = 148$ W m^{-1} K^{-1}) with water ($k_f = 0.609$ W m^{-1} K^{-1}) as the working fluid ($k_s/k_f = 243$). For illustration purposes, we depict in Fig. 5 the temperature distribution for a channel with aspect ratio $A = 3$, $w_c/w = 0.3$ and $h = 1.1$. The boundaries between the solid and the liquid are clearly visible due to the large, discontinuous change in the temperature gradient at this interface. Due to the solid's high thermal conductivity, the temperature gradients in the solid are relatively small and the temperature distribution resembles an almost isothermal one. The solid's temperature is likely to get even closer

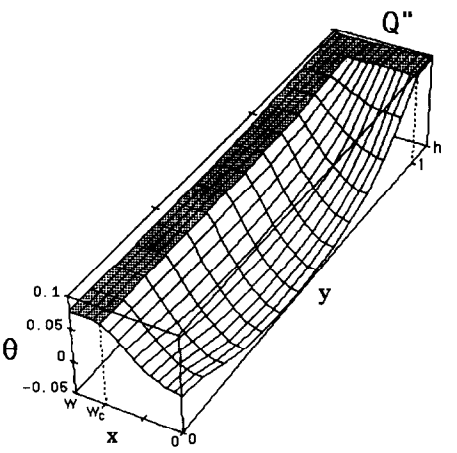

FIG. 5. Cross-sectional temperature distribution for $k_s/k_f = 243$, $A = 3$, $w_c/w = 0.3$, and $h = 1.09$. The boundary $y = h$ is exposed to a uniform heat flux.

to an isothermal distribution when the fluid's thermal conductivity decreases as would be the case if refrigerants or gases were used as coolants. Note that the temperature distribution in the fin varies almost linearly as a function of the fin's height rather than exponentially as in classical fin analysis.

Next, we calculated the local heat transfer coefficient along the solid–liquid interface. In Fig. 6, we show the local Nusselt number (Nu_L) as a function of location along the base's and fin's surfaces for $w_c/w = 0.5$, $h = 1.11$, $k_s/k_f = 243$, and aspect ratios 2, 4, and 9. In each case, the local Nusselt number is normalized with its maximum value. To facilitate comparison of the various geometrical configurations, the distance along the channel's width is measured as a fraction of w_c. Figure 6 is qualitatively similar to results presented in ref. [18]. Not surprisingly, the local Nusselt number assumes minimal values at the channel's corners where the local velocities and their

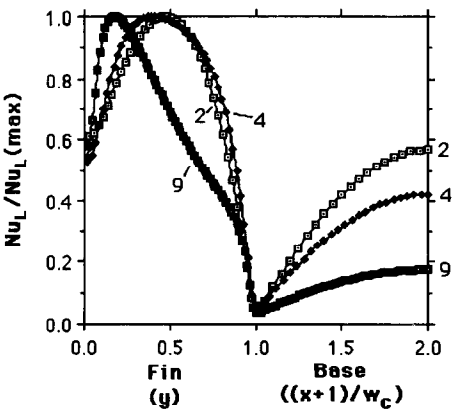

FIG. 6. The local Nusselt number (Nu_L), normalized with its maximum value, is depicted as a function of position along the channel walls (fin and base). The length along the base is shown as a fraction of w_c. Results are shown for $w_c/w = 0.5$, $h = 1.11$, $k_s/k_f = 243$, and aspect ratios 2 (hollow squares), 4 (diamonds), and 9 (filled squares).

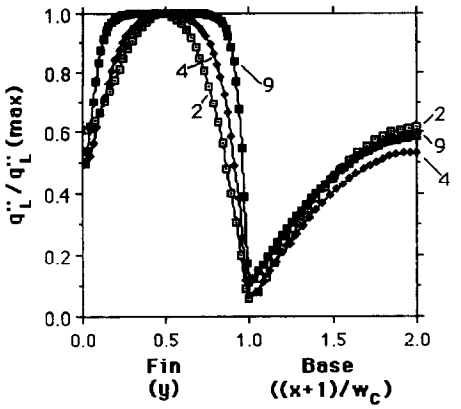

FIG. 7. The local heat flux (q_L), normalized with its maximum value, is depicted as a function of position along the channel walls (fin and base). The length along the base is shown as a fraction of w_c. Results are shown for $w_c/w = 0.5$, $h = 1.11$, $k_s/k_f = 243$, and aspect ratios 2 (hollow squares), 4 (diamonds), and 9 (filled squares).

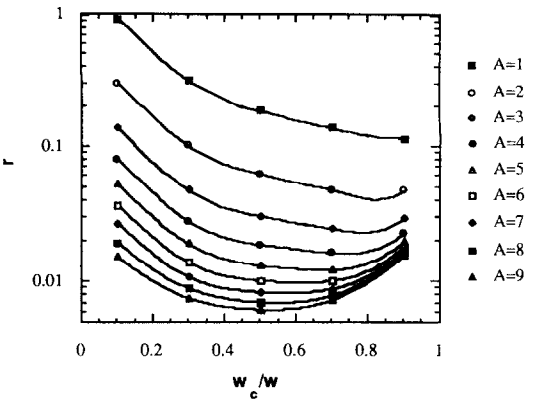

FIG. 8. Dimensionless thermal resistance as a function of w_c/w and aspect ratio for $h = 1.11$ and $k_s/k_f = 243$.

gradients are the smallest. The local Nusselt number attains a local maximum at the base's center and along the fin at $y = y_c < 0.5$, where y_c decreases with increasing aspect ratio. Although the velocity profile is symmetric with respect to the fin's mid-height ($y = 0.5$), the same is not true with respect to Nu_L. Two factors conspire to create the asymmetry in Nu_L. First of all, the temperature at $y < 0.5$ is lower than that at $y > 0.5$ and, second, due to the insulated top boundary at $y = 0$, more heat is transferred into the fluid from the upper half of the fin ($y < 0.5$) than would have occurred if the fin, say, were infinite in length.

The effect of the latter factor is further illustrated in Fig. 7, which depicts the local heat flux (q_L'') as a function of location along the fin's and channel's base. The abscissa and the geometrical configurations in Fig. 7 are identical to those in Fig. 6. The ordinate of Fig. 7 is the local heat flux normalized with its maximum value in each case. Note that the heat flux profile is relatively flat (especially in the high aspect ratio case) along a substantial fraction of the fin's length.

Figures 5–7 demonstrate the inadequacy of the classical fin analysis employed by many researchers (see, for example refs. [8, 15–17]), which assumes a uniform heat transfer coefficient and predicts an exponentially decaying temperature along the fin's length. The aforementioned researchers have also neglected the heat transfer along the base. Figures 6 and 7 provide an estimate of the error resulting from neglecting this factor. For example, in Fig. 7, the base contributes, 2.5, 5.3, and 12% respectively, of the total heat transfer for aspect ratios 9, 4, and 2. As this indicates, neglecting the base's contribution to the total heat transfer may be justified only for channels with high aspect ratios.

Figures 8 and 9 depict the non-dimensional thermal resistance r as a function of the channel's relative width (w_c/w) and the cross-section's height (h) for aspect ratios ranging from 1 to 9. The figures illustrate that the thermal resistance decreases monotonically with increasing aspect ratio. The rate of decrease diminishes as the aspect ratio reaches the point of diminishing returns at around 8.

Figure 8 illustrates that the resistance attains a minimum value for a certain w_c/w ratio. As the aspect ratio increases, this value decreases and approaches asymptotically 0.5. That is, for large aspect ratios, minimum resistance is obtained when the channels and fins have the same width. This accords with Tuckerman's [8] results.

In Fig. 9, we show the thermal resistance as a function of the non-dimensional cross-section's height (h). In other words, the figure depicts the effect of the substrate's thickness on the thermal resistance. Clearly, the thermal resistance decreases monotonically as the substrate's thickness is reduced. The minimal substrate thickness should be determined by structural considerations. The curves in Fig. 9 appear to be similar and they can be conveniently correlated by

$$r - r_{h=1.11} = \frac{k_f}{k_s}(h - 1.11), \tag{14}$$

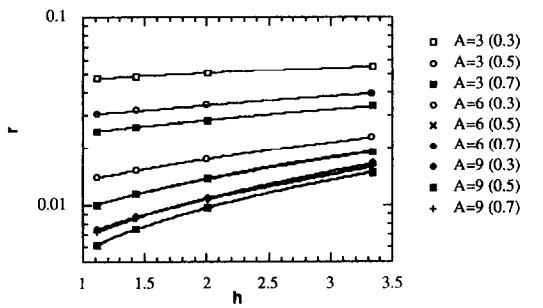

FIG. 9. Dimensionless thermal resistance as a function of h and the aspect ratio for $k_s/k_f = 243$. The numbers in parentheses indicate the w_c/w value in each case.

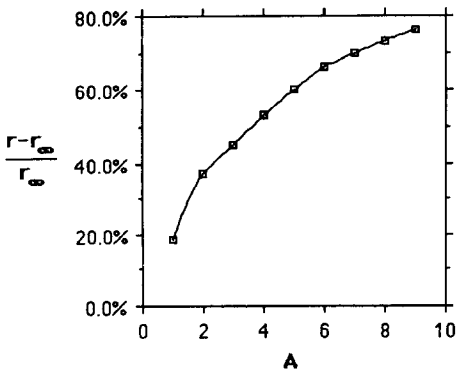

FIG. 10. The relative difference between the actual resistance and the isothermal approximation for $h = 1.11$ and $k_s/k_f = 243$.

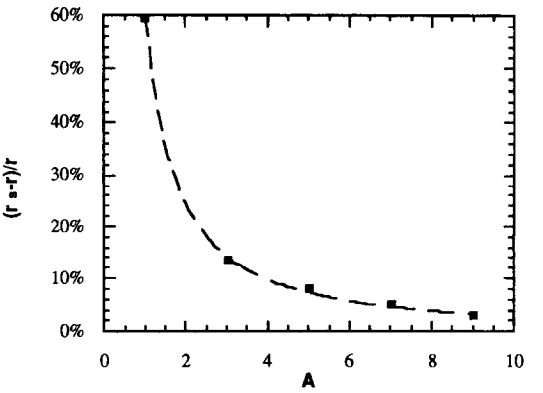

FIG. 11. The relative difference between Samalam's prediction for an 'optimal geometry' thermal resistance and our numerical result for the same geometry is depicted as a function of aspect ratio.

where $r_{h=1.11}$ is the resistance at $h = 1.11$. For the cases shown in Fig. 9, equation (14) is accurate within 2%. Equation (14) suggests that the heat conduction in the base is essentially one-dimensional. The value of this equation is that it allows one to calculate the resistance for a single value of h (i.e. Fig. 8) and subsequently generalize the result for other h values.

Next we compare our computational results with the limiting case of infinite solid thermal conductivity, i.e. $k_s \to \infty$ ($k_s/k_f \to \infty$). In this case, the solid phase exhibits zero resistance and the temperature in it is isothermal. Therefore, the predictions of this limiting case model should provide a lower bound for the thermal resistance. The heat transfer in rectangular ducts with three isothermal sides has been investigated in the heat transfer literature and the results are compiled in ref. [23]. Figure 10 depicts the relative difference between our calculated results (r) and the isothermal approximation (r_∞) for $k_s/k_f = 243$ and $h = 1.11$. Note that $(r-r_\infty)/r_\infty$ increases as the aspect ratio increases. This is expected since as the fin's length increases, so does its temperature non-uniformity.

Finally, we compare our results with the theoretical and experimental results of previous workers. Below, using our notation, we reproduce Samalam's [17] expression for the fully developed resistance (r),

$$r_{\text{Samalam}} = \frac{w}{w_c}\frac{1}{A^2\,Nu} + \frac{k_f}{k_s}\frac{1}{3\left(1-\dfrac{w_c}{w}\right)}, \qquad (15)$$

in which Samalam has chosen $Nu = 6.5$. Samalam's [17] and our thermal resistances are compared in Fig. 11 for identical channels in a 1 cm wide, 1 cm long silicon chip cooled with water with a 213.7 kPa pressure drop. We chose to compare our data with Samalam's as his solution is more complete than the ones available in refs. [8, 16]. The deviations between our calculations and Samalam's predictions decrease as the channel's aspect ratio increases. Given the approximations used in Samalam's model, his predictions appear to perform surprisingly well.

Next, we compare our predictions with experimental data available in the literature for microchannels etched in silicon. We examined closely data reported in refs. [2, 8, 12]. Comparison was possible only with Tuckerman's data [2, 8]. Kishimoto and Sasaki [12] did not provide sufficient information to allow the reduction of their data to the necessary form and attempts to interpret their data resulted in inconsistent predictions for the thermal resistance.

The structures tested by Tuckerman and his experimental results are described in Table 1 together with the predictions from both our and Samalam's models. Tuckerman's devices consisted of 1 cm × 1 cm heated areas transferring heat to channels in silicon chips that were 2 cm long and 1.5 cm wide in Case 1, and 1.4 cm long and 2 cm wide in Cases 2, 3, and 4. In all cases, the working fluid was water. For the theoretical predictions, all material properties were evaluated at room temperature.

With the exception of Case 1, the theoretical predictions and experimental observations are in rough agreement (better than 20%). Due to the vast difference between the experimental result of Case 1 and the other cases, we suspect a possible error in the reported data. The differences between the experimental observations and the theoretical predictions in the other three cases might be attributable to a number of factors. For instance, in the experiments, only a part of the chip's surface was heated, resulting in somewhat non-uniform heating, in contrast to the uniform heating in the theoretical model. Also, in the experiments, the pyrex cap may have participated in the thermal process while the model assumes a perfect insulator. Additionally, in the experiments, part of the heating power may have been lost to the ambient rather than transferred to the channel. Finally, a thermal development length at the channel's inlet (not included in the model) may have resulted in a higher heat transfer coefficient along this section of the channel. To examine this last effect, Tuckerman ran a few experiments with configuration 4, demonstrating that the thermal

Table 1. Comparison of Tuckerman's experimental thermal resistance values (°C W^{-1}) with our theoretical predictions

Case	Reynolds number	Experiment	Our calculations	Samalam
1	121	0.151	0.089	0.084
2	280	0.059	0.074	0.067
3	426	0.076	0.071	0.070
4	547	0.062	0.064	0.062

Case	Channel width ($2W_c$) (μm)	Wall width ($2(W-W_c)$) (μm)	Channel depth (H_c) (μm)	Chip thickness (H) (μm)	Pressure drop (psi)	Flow rate (cm^3 s^{-1})	Heating rate (Q'') (W cm^{-2})
1	64	36	280	489	15	1.86	34.6
2	56	44	320	533	15	4.7	181
3	55	45	287	430	17	6.5	277
4	50	50	302	458	31	8.6	790

resistance was invariant with flow rate and that the development length does not play a significant role.

Despite its shortcomings, the comparison of the theoretical predictions with the experimental data demonstrates that the model provides a realistic prediction of the thermal resistance.

5. DESIGN FORMULATION

In this section, we describe algorithms for selecting the dimensions and number of channels to yield minimal thermal resistance for the given working fluid, wafer dimensions (i.e. W_T, H, and L), and operating constraints such as the available pumping power or pressure drop and maximum allowed rise in the bulk temperature.

We begin by calculating the pressure drop and the pumping power. For fully developed, laminar flow in a uniform cross-section duct, $C(A) = f \cdot Re$, where f is the Moody friction factor, $Re = \rho_f \bar{U} D_H / \mu$ is the Reynolds number, μ is the fluid's viscosity, and $C(A)$ is a tabulated constant [23] which depends only on the channel's geometry. The pressure drop across the channel's length (L) is

$$\Delta p = \frac{C \mu \bar{U} L}{2 d_h^2 H_c^2}, \tag{16}$$

and the corresponding power required to pump fluid through n channels is:

$$P_T = n \bar{U} (2 H_c W_c) \Delta p. \tag{17}$$

We assume that the maximum rise in the bulk (ΔT_B) temperature is given and that the designer selects a channel with maximum depth H_c as allowed by structural considerations. In such a case, the various channel dimensions satisfy the equation:

$$\frac{w}{w_c} \frac{C}{d_H^2} = \beta_1, \tag{18}$$

where

$$\beta_1 = \frac{2 \rho_f C_p \Delta T_B \Delta p}{Q'' \mu L^2} H_c^3$$

for the given pressure drop and

$$\beta_2 = \left(\frac{\rho_f C_p \Delta T_B}{Q'' L} \right)^2 \frac{2 P_T}{\mu W_T L} H_c^3,$$

for the given pumping power. To select the optimal dimensions for the heat exchanger, we superimpose the constraint curve described by equation (18) onto Fig. 9. These curves represent the channel dimensions which satisfy the aforementioned constraints. The dimensions to be selected are those which correspond to minimal thermal resistance.

For illustration purposes, consider a 450 μm thick silicon wafer, with a heated area of 1 cm × 1 cm and a uniform flux of 2×10^6 W m^{-2}, which is to be cooled with water ($C_p = 4.18$ kJ kg^{-1} K^{-1}, $\rho_f = 997.1$ kg m^{-3}, $\mu = 0.00089$ N s^{-1} m^{-2}, $k_f = 0.609$ W m^{-1} °C^{-1}). The pressure drop and the rise in the bulk temperature are restricted to 68.95 kPa (10 psi) and 15°C, respectively. In Fig. 12, we superimpose (dashed line) on Fig. 9 the surface described by equation (18)

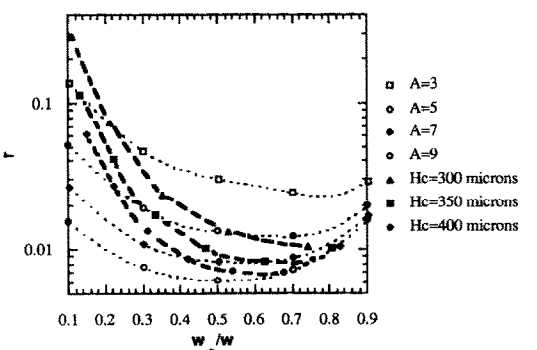

FIG. 12. A plot of allowable design configurations given the constraints in the example (thick dashed lines) together with some of the Fig. 8 curves (thin dotted lines).

for channel depths $H_c = 300$, 350, and 400 μm. The designer should select the geometry for which the constraints (dashed) curve attains minimal thermal resistance.

Alternatively, one may wish to minimize the pumping power for a given, allowed temperature difference between the exit's surface temperature and the entrance temperature (i.e. R^* is specified). To this end, one may minimize the pumping power, specified as a function of the channel's geometry, as stated below

$$P_T = \frac{L\mu}{8\rho_f^2 C_p^2 W_T H_c^3}\left(\frac{w}{w_c}\right)\frac{(1+A)^2 C(A)}{(R^*-R)^2}. \quad (19)$$

In the above, R is given implicitly as a function of the cross-sectional geometry through graphs such as Fig. 9.

6. CONCLUSIONS

Advances in microfabrication technology allow us to fabricate minute channels in silicon wafers and other suitable materials. These minute channels can be integrated into extremely efficient, low mass, low thermal resistance, micro-heat exchangers. Thermal resistances of 0.1°C W^{-1} or smaller are attainable. Although such heat exchangers can be used in a variety of applications, the nearest term, potential use of these micro-heat exchangers is probably in the area of electronic cooling. Accordingly, we have studied theoretically the thermal resistance of cooling channels integrated into silicon chips and have devised a design procedure for the selection of channel dimensions in conformity with operational constraints. We have compared our results with approximate studies available in the literature and we have assessed the validity of assumptions made by previous investigators.

Acknowledgment—The research reported in this paper has been supported by the National Science Foundation through grant CTS 90-12904.

REFERENCES

1. D. B. Tuckerman and R. F. W. Pease, High performance heat sinking for VLSI, *IEEE Electron Device Lett.* **EDL-2,** 126 (1981).
2. D. B. Tuckerman and R. F. W. Pease, Optimized convective cooling using micromachined structures, *J. Electrochemical Society* **129**(3), C98 (1982).
3. P. Wu and W. A. Little, Measurement of the heat transfer characteristics of gas flow in fine channel heat exchangers used for microminiature refrigerators, *Cryogenics* 415–419 (August 1984).
4. G. W. Swift, A. Migliori and J. C. Wheatley, Microchannel crossflow fluid heat exchanger and method for its fabrication, US patent 4,516,632 (1985).
5. W. Bier, W. Keller, G. Linder, D. Seidel and K. Schubert, Manufacturing and testing of compact micro heat exchanger with high volumetric heat transfer coefficients. In *Microstructures, Sensors and Actuators* (Edited by D. Cho, R. Warrington, C. Blechinger, A. Pisano, W. Trimmer and L. Trefethan), DSC-Vol. 19, pp. 189–197. ASME, New York (1990).
6. K. E. Petersen, Silicon as a mechanical material, *Proc. IEEE* **70,** 420–457 (1982).
7. T. L. Hoopman, Microchanneled structures. In *Microstructures, Sensors and Actuators* (Edited by D. Cho, R. Warrington, C. Blechinger, A. Pisano, W. Trimmer and L. Trefethan), DSC-Vol. 19, pp. 171–174. ASME, New York (1990).
8. D. B. Tuckerman, Heat-transfer microstructures for integrated circuits, Ph.D. thesis, Stanford University (1984). (Also Lawrence Livermore National Laboratory, UCRL-53515.)
9. N. Goldberg, Narrow channel forced air heat sink, *IEEE Trans. Components, Hybrids, Manufacturing Tech.* **CHMT-7**(1), 154–159 (1984).
10. D. Nayak, L. Hwang, I. Turlik and A. Reisman, A high performance thermal module design for computer packaging, *J. Electronic Mater.* **16,** 357–364 (1987).
11. L. Hwang, I. Turlik and A. Reisman, A thermal module design for advanced packaging, *J. Electronic Mater.* **16,** 347–355 (1987).
12. S. Sasaki and T. Kishimoto, Optimal structure for microgrooved cooling fin for high power LSI devices, *Electronics Lett.* **22,** 1332–1333 (1986).
13. M. Mahalingam, Thermal management in semiconductor device packaging, *Proc. IEEE* **73,** 1396–1404 (1985).
14. M. Mahalingam and J. Andrews, High performance cooling for microelectronics. In *Cooling Technology for Electronic Equipment* (Edited by W. Aung), pp. 139–155. Hemisphere, New York (1988).
15. R. J. Philips, Microchannel heat sinks. In *Advances in Thermal Modeling of Electronic Components and Systems* (Edited by A. Bar-Cohen and A. D. Kraus), Vol. 2, pp. 109–184. ASME, New York (1990).
16. R. W. Keyes, Heat transfer in forced convection through fins, *IEEE Trans. Electronic Devices* **ED-31**(9), 1218–1221 (1984).
17. V. K. Samalam, Convective heat transfer in microchannels, *J. Electronic Mater.* **18,** 611–617 (1989).
18. E. M. Sparrow, B. R. Baliga and S. V. Patankar, Forced convection heat transfer from a shrouded fin array with and without tip clearance, *Trans. ASME, J. Heat Transfer* **100,** 572–579 (1978).
19. J. Pfahler, J. Harley, H. H. Bau and J. Zemel, Gas and liquid flow in small channels. In *ASME WAM 91 Proceedings, Symposium on MicroMechanical Systems* (to appear).
20. F. M. White, *Viscous Fluid Flow*, p. 123. McGraw-Hill, New York (1974).
21. K. M. Kelkar, Iterative method for the numerical prediction of heat transfer in problems involving large differences in thermal conductivities, *Numerical Heat Transfer B* **17,** 113–128 (1990).
22. A. Weisberg, H. H. Bau and J. Zemel, Micro-heat exchangers. In *Microstructures, Sensors and Actuators* (Edited by D. Cho, R. Warrington, C. Blechinger, A. Pisano, W. Trimmer and L. Trefethan), DSC-Vol. 19, pp. 159–170. ASME, New York (1990).
23. R. K. Shah and A. L. London, *Laminar Flow Forced Convection in Ducts.* Academic Press, New York (1978).

ANALYSE DES MICROCANAUX POUR LE REFROIDISSEMENT INTEGRE

Résumé—Des progrès récents dans l'usinage précis de petits canaux ont rendus possibles l'utilisation de tels microcanaux dans des échangeurs thermiques extrêmement compacts, très efficaces qui permettent des flux thermiques très élevés avec des petites résistances thermiques. Par exemple, de tels microcanaux peuvent être réalisés directement sur l'arrière des chips électroniques pour permettre le refroidissement de ces chips. On analyse de tels échangeurs en résolvant numériquement un problème thermique conjugué qui consiste en la détermination simultanée des champs de température, à la fois dans le substrat solide et dans le fluide. En outre, on présente un algorithme de conception pour le choix des dimensions de l'échangeur thermique.

UNTERSUCHUNG VON MIKROKANÄLEN FÜR INTEGRIERTES KÜHLEN

Zusammenfassung—Neue Fortschritte in der Herstellungsgenauigkeit von kleinen Kanälen machen die Verwendung solcher Mikrokanäle in ultrakompakten und hocheffizienten Wärmeüberträgern möglich, die das große Verhältnis von Oberfläche zu Volumen ausnutzen um große Wärmestromdichten mit kleinen thermischen Widerständen zu transportieren. Solche Mikrokanäle können z. B. direkt in die Rückseite von elektronischen Chips eingearbeitet werden um die Kühlung dieser Chips zu verbessern. In der vorliegenden Arbeit werden derartige Wärmeaustauscher durch numerische Behandlung des konjugierten Wärmeübergangsproblems untersucht, das in der simultanen Bestimmung der Temperaturfelder im festen Substrat und in Fluid besteht. Zusätzlich stellen wir einen Algorithmus zur Dimensionierung derartiger Wärmeaustauscher vor.

АНАЛИЗ ПРИМЕНЕНИЯ МИКРОКАНАЛОВ ДЛЯ ОХЛАЖДЕНИЯ

Аннотация—Последние достижения в области точной обработки малых каналов позволили применять такие микроканалы в сверхкомпактных высокоэффективных теплообменниках, когда отношение площади поверхности каналов к объему велико, так что перенос больших тепловых потоков осуществляется с малыми тепловыми сопротивлениями. В частности, такие микроканалы могут монтироваться непосредственно на обратной стороне электронных чипов с целью их охлаждения. В настоящем исследовании рассматриваемые теплообменники анализируются на основе численного решения сопряженной задачи теплопереноса, позволяющего определить температурные поля в твердой подложке и жидкости. Кроме того, приводится расчетный алгоритм для выбора размеров теплообменников.